JOURNAL OF PROPULSION AND POWER
Vol. 41, No. 5, September–October 2025

Correlation for Restart Boundaries of Simplified Two-Dimensional Hypersonic Inlets

Xiao-Tong Tong,* Lian-Jie Yue,† Hao Chen,‡ Wan-Nan Wu,§ and Qi-Fan Zhang¶
Chinese Academy of Sciences, 100190 Beijing, People's Republic of China
and
Zheng Chen**
Peking University, 100871 Beijing, People's Republic of China

https://doi.org/10.2514/1.B39815

The restart ability is a significant concern in the design of hypersonic inlets, but existing theoretical and empirical formulas can hardly accurately predict the restart characteristics. To develop a universal rapid prediction method, this paper explores the similarity law of the restart phenomenon at variable Mach numbers based on systematic numerical simulation. The corrected contraction angle and internal contraction ratio (ICR) that reflect the influence of multiple geometric and aerodynamic parameters are proposed, and an empirical formula for restart boundaries is established and validated by the literature data. It is revealed that the restart boundaries obey an inherent geometric similarity law, and the discrete relation between Mach number and ICR, emphasized by most existing studies, is not essential. The restart-critical wall pressure characteristics are analyzed, and a self-similar pressure criterion is obtained with the incident shock strength considered.

Nomenclature

A	=	area, m^2
b	=	empirical parameter
C_f	=	coefficient of wall friction
d	=	empirical parameter
E	=	total energy, J/kg
e	=	internal energy, J/kg
f	=	function
h_c	=	cowl lip height, mm
h_{ce}	=	equivalent cell size, mm
h_t	=	geometric throat height, mm
ICR	=	internal contraction ratio
ICR_{eff}	=	effective internal contraction ratio
ICR_{effM}	=	corrected internal contraction ratio
k	=	turbulent kinetic energy, m^2/s^2
L_c	=	cowl length, mm
L_c^*	=	dimensionless cowl length
L_f	=	length of upstream plate, mm
M	=	Mach number
N_{cell}	=	number of cells
p	=	static pressure, kPa
$p_{max\text{-}re}$	=	critical wall pressure peak, kPa
S	=	start ability index
S_μ	=	Sutherland constant
T	=	temperature, K
u	=	velocity, m/s
x	=	X-coordinate, mm
α	=	empirical parameter
β	=	shock angle, deg
γ	=	specific heat ratio Φ
δ_c	=	entrance boundary-layer thickness, mm
δ_c^*	=	entrance displacement thickness, mm
θ_c	=	contraction angle, deg
θ_{cM}	=	corrected contraction angle, deg
$\theta_{re\text{-}pl}$	=	platform of restart cowl angle, deg
μ	=	dynamic viscosity, kg/(m · s)
ρ	=	density, kg/m^3
σ_{ij}	=	molecular viscous stress, Pa
Φ	=	function
ω	=	specific turbulence dissipation rate, s^{-1}

Subscripts

eff	=	effective quantity
max	=	pressure peak
re	=	restart boundary
rec	=	restart critical state
recM	=	corrected critical value
s	=	value of separation shock
0	=	reference value
1, 2	=	value before/behind cowl shock
∞	=	freestream condition

Received 29 September 2024; accepted for publication 4 July 2025; published online 30 July 2025.

*Research Associate, State Key Laboratory of High-Temperature Gas Dynamics, Institute of Mechanics; also College of Mechanics and Engineering Science, Peking University, 100871 Beijing, People's Republic of China.
†Professor, State Key Laboratory of High-Temperature Gas Dynamics, Institute of Mechanics; also University of Chinese Academy of Sciences, 100049 Beijing, People's Republic of China; yuelj@imech.ac.cn (Corresponding Author).
‡Associate Professor, State Key Laboratory of High-Temperature Gas Dynamics, Institute of Mechanics.
§Assistant Professor, State Key Laboratory of High-Temperature Gas Dynamics, Institute of Mechanics.
¶Associate Professor, Institute of Mechanics; zhangqifan@imech.ac.cn (Co-Corresponding Author).
**Professor, State Key Laboratory for Turbulence and Complex Systems, College of Mechanics and Engineering Science.

I. Introduction

THE hypersonic inlet has two operating states: the started and the unstarted [1,2]. The unstart phenomenon, accompanied by a catastrophic growth of boundary-layer separation, can decrease the captured mass flow rate, increase thermal loads, and even cause flight failure. Hence the restart (switching from unstarted state to started state) ability is a major concern in inlet design. As shown in Fig. 1, the restart phenomenon features as the regression of a massive separation region. After extensive studies on restart boundary and mechanism [3], researchers have realized that the restart characteristics of hypersonic inlets depend on the internal contraction section, and the dominant mechanism is shock-wave/boundary-layer interaction (SWBLI) [4,5], which differs from the supersonic inlets with small internal contraction angles [6].

The restart ability can be improved by the auxiliary means such as variable geometry [7–10], boundary-layer bleeding [11–13], and mass injection [4,14]. These control strategies depend on an accurate prediction of the restart boundary, from which the required mechanical control quantity or suction/injection mass flow rate can be calculated. However, there is not a universal estimation method because the restart phenomenon is affected by both incoming flow condition and geometric configuration of the inlet. As a result, a lot of numerical simulation and wind tunnel tests are needed in the design of scramjets, raising development cost.

The existing rapid prediction methods for the restart boundary can be divided into three categories:

1) Kantrowitz equations

Kantrowitz theory [15] is based on a hypothetical critical starting flow regime: a normal shock wave stands at the entrance of the contraction duct, and the gas reaches sonic speed at the throat. The restart internal contraction ratio (ICR) is

$$\left(\frac{A_c}{A_t}\right)_{\text{Kantrowitz}} = \sqrt{\frac{\gamma+1}{2+(\gamma-1)M_\infty^2}} \cdot M_\infty^{\frac{\gamma+1}{\gamma-1}} \cdot \left(\frac{2\gamma}{\gamma+1}M_\infty^2 - \frac{\gamma-1}{\gamma+1}\right)^{\frac{1}{1-\gamma}} \tag{1}$$

where A_c and A_t are the entrance and throat area of the contraction duct, respectively. For two-dimensional cases, the entrance and the throat height, h_c and h_t, are used, as illustrated in Fig. 1. As shown in Fig. 2, the Kantrowitz equation cannot predict the highly discrete restart boundaries. The reason is that the normal shock hypothesis does not match the actual oblique-shock-wave/boundary-layer interaction, and the Reynolds number effect is ignored. Subsequent studies extend Kantrowitz's theory by considering the cowl shock strength [16], curved compression surface [17], and external shock waves [18,19]. These studies have great theoretical significance, but the prediction methods still cannot meet the engineering demands.

2) Theoretical models of SWBLI

Another routine is theoretical modeling for SWBLI in the contraction duct, and thus the criteria for the regression of massive separation region can be determined. Xie [20] and Yang [21] have made positive attempts. However, their work oversimplifies the flow structure by assuming the separation-shock-on-lip regime as the only critical flow regime. Other researchers have reported the critical state with a separation shock detached from the cowl lip [22–28]. In addition, the existing models adopt a rough formula for the pressure downstream of the separation region [20] and the separation shock [21], which may lead to a narrow applicability considering the various flow conditions [29–33].

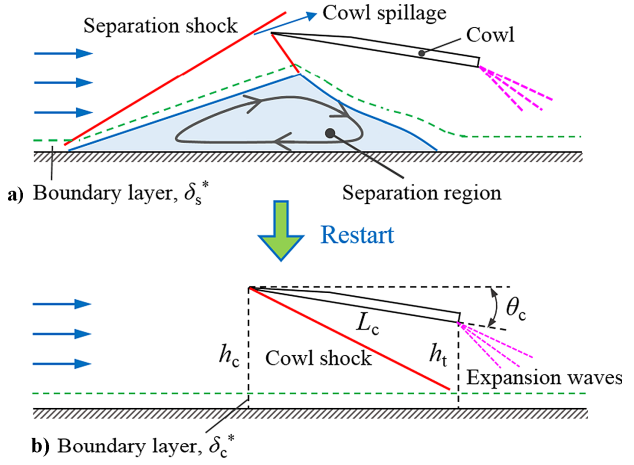

Fig. 1 Restart phenomenon in a contraction duct: a) unstarted state; b) started state.

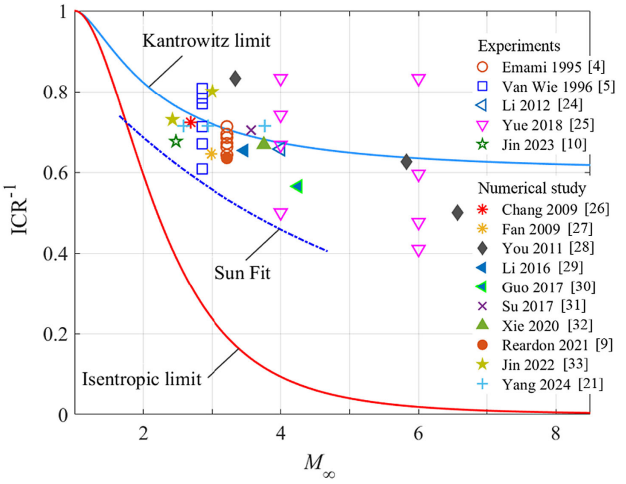

Fig. 2 Restart boundaries in the literature comparing to prediction formulas [4,5,9,10,21,24–33].

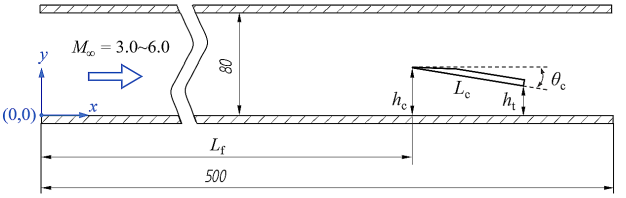

Fig. 3 Schematic physical model of a simplified contraction duct (Ref. [38]).

3) Empirical formulas

Considering the complexity of SWBLI theories, researchers have been seeking empirical formulas for the restart boundaries. Mölder [34] proposed the startability index S, which is essentially a linear interpolation between the Kantrowitz limit and the isentropic limit:

$$\left(\frac{A_t}{A_c}\right) = (1-S)\left(\frac{A_t}{A_c}\right)_{\text{Isentropic}} + S\left(\frac{A_t}{A_c}\right)_{\text{Kantrowitz}} \tag{2}$$

Here the isentropic limit is

$$\left(\frac{A_c}{A_t}\right)_{\text{Isentropic}} = \frac{1}{M_\infty}\left(\frac{2}{\gamma+1} + \frac{\gamma-1}{\gamma+1}M_\infty^2\right)^{\frac{\gamma+1}{2(\gamma-1)}} \tag{3}$$

Analogous to Van Wie's formula for unstart boundaries [2], Sun [35] developed a formula for self-starting (restart) boundaries, representing the restart ICR as a function of the entrance Mach number:

$$\left(\frac{A_c}{A_t}\right)_{\text{re}} = 0.933 + \frac{M_c}{6.87} + \frac{M_c^2}{40.9}, \qquad 1.65 < M_c < 4.68 \tag{4}$$

In Fig. 1, Sun's formula can be regarded as a bottom boundary for the data points in the literature. Nevertheless, Eqs. (2–4) are only capable of rough estimates because they ignored the effects of contraction angle [36] and Reynolds number [37].

To overcome these defects, our previous studies [23,38] proposed a similarity law based on the dimensionless cowl length L_c^* and effective contraction ratio ICR_{eff}:

$$L_c^* = \frac{L_c}{h_c - \delta_c^*} \tag{5}$$

$$\text{ICR}_{\text{eff-re}}^{-1} = \frac{h_t - \delta_t^*}{h_c - \delta_c^*} = 1 - L_c^* \sin\theta_{\text{re}} \tag{6}$$

Here L_c, h_c, and δ_c^* are the cowl wedge length, entrance height of the contraction duct, and the displacement boundary-layer thickness at the cowl-lip position, as marked in Fig. 1. In Eqs. (5) and (6), δ_c^* in the started state is adopted, which is essentially an approximation to the characteristic displacement thickness near the separation point in the unstarted state, δ_s^*. This is because the horizontal direction distance between the unstarted separation point and the cowl lip, x_c–x_s, is usually much smaller than the upstream plate length, leading to a negligible difference between δ_c^* and δ_s^*.

L_c^* is analogous to the startability index S in mathematical properties, but L_c^* has clear physical implications. The self-similar empirical formula based on L_c^* and $\mathrm{ICR_{eff}}$ is proved to be valid for fixed Mach numbers. Nevertheless, there are multiple empirical parameters depending on the Mach number in the formula, making it inconvenient for variable Mach number situations. To develop a prediction method balancing accuracy and practicality for the restart phenomenon, this paper explores a more universal restart similarity law based on the numerical simulation results. The similarity quantities that reflect the Mach number effect are constructed, and the wall pressure characteristics of the restart phenomenon are analyzed.

II. Numerical Method

A. Physical Model and Governing Equations

Figure 2 shows the physical model used in the numerical simulation, which is consistent with Van Wie's experiment [5]. The wedge plate and the bottom flat plate form a contraction duct, and the cowl can rotate anticlockwise around its leading edge, thus decreasing the contraction angle θ_c and ICR. The supersonic airflow enters the computational domain from the left. Table 1 lists the inflow conditions, where the cowl lip Mach number of 3–6 corresponds to the flight Mach number of 5–9. The incoming static temperature is 107.7 K, which is the same as the experiment condition [5]. The freestream turbulence intensity and turbulence length scale are 4.5% and 5 mm, respectively. All the walls are adiabatic. The thickness and displacement thickness of the entrance boundary layer depend on the Reynolds number, and the characteristic length of the Reynolds number is the length of the upstream flat plate, L_f, which is fixed at 279.4 mm. Please note that $h_c/\delta_c^* = 4 \sim 20$ or $h_c/\delta_c = 2 \sim 8$ is determined in the started state, and δ_c^* cannot reach the entrance height h_c, which accords with the value range in practical flight ($h_c/\delta_c = 5 \sim 10$) and wind-tunnel conditions ($h_c/\delta_c = 1.1 \sim 3.9$ [5]; $4.5 \sim 16.7$ [25]).

The finite volume method is used to solve the two-dimensional compressible Reynolds-averaged Navier–Stokes equations. In Cartesian coordinates, the governing equations may be written as

$$\frac{\partial \bar{\rho}}{\partial t} + \frac{\partial}{\partial x_i}\left(\bar{\rho}\tilde{u}_i\right) = 0 \tag{7}$$

$$\frac{\partial}{\partial t}\left(\bar{\rho}\tilde{u}_i\right) + \frac{\partial}{\partial x_j}\left(\bar{\rho}\tilde{u}_j\tilde{u}_i\right) = -\frac{\partial \bar{p}}{\partial x_i} + \frac{\partial}{\partial x_j}\left(\tilde{\sigma}_{ij} - \overline{\rho u_j'' u_i''}\right) \tag{8}$$

$$\frac{\partial}{\partial t}\left(\bar{\rho}\tilde{E}\right) + \frac{\partial}{\partial x_j}\left[\bar{\rho}\tilde{u}_j(\tilde{E} + \bar{p})\right] = \frac{\partial}{\partial x_j}\left[\tilde{u}_i(\tilde{\sigma}_{ij} - \overline{\rho u_j'' u_i''})\right] + \frac{\partial}{\partial x_j}\left(\kappa\frac{\partial \tilde{T}}{\partial x_j}\right) + \frac{\partial}{\partial x_j}\left(-c_p\overline{\rho u_j'' T''} + \overline{u_i''\sigma_{ij}} - \frac{1}{2}\overline{\rho u_j'' u_i'' u_i''}\right) \tag{9}$$

Table 1 Boundary-layer characteristics at the entrance under different conditions

No.	M_∞	p_∞, kPa	Re_{xc}, 10^7	δ_c, mm	δ_c^*, mm
1	3.0	18.77	1.433	4.82	1.52
2	3.0	9	0.687	5.10	1.57
3	3.0	30	2.290	4.60	1.25
4	4.0	18.77	1.910	4.61	1.66
5	5.0	18.77	2.388	4.38	1.91
6	6.0	18.77	2.967	4.11	2.15

in which $\bar{\rho}$, $\tilde{u}_i$ $\bar{p}$, $\tilde{E}$, and $\tilde{\sigma}_{ij}$ are density, velocity, pressure, total energy, and viscous stress tensor with the overbar and tilde representing the time-averaged values and representing mass-averaged values, respectively. For a perfect gas, the equation of state and the total energy are

$$\bar{p} = (\gamma - 1)\bar{\rho}\tilde{e} \tag{10}$$

$$\tilde{E} = \tilde{e} + \frac{1}{2}\tilde{u}_i\tilde{u}_i + k \tag{11}$$

Herein $\tilde{e} = c_v\tilde{T}$ is the specific internal energy for calorically a perfect gas, and k is the turbulent kinetic energy, and c_p and c_v are the specific heat capacities at constant pressure and volume, respectively. The real-gas effect can be ignored at relatively low temperatures, and hence the calorically perfect gas model with a specific heat ratio γ of 1.4 is used.

Based on the constitutive model of Newtonian fluid, the mean molecular viscous stress is given by

$$\tilde{\sigma}_{ij} = \mu\left(\frac{\partial \tilde{u}_i}{\partial x_j} + \frac{\partial \tilde{u}_j}{\partial x_i} - \frac{2}{3}\frac{\partial \tilde{u}_k}{\partial x_k}\delta_{ij}\right) \tag{12}$$

The molecular viscosity μ depending on temperature is solved with Sutherland's formula:

$$\frac{\mu}{\mu_0} = \left(\frac{T}{T_{0\mu}}\right)^{1.5}\frac{T_{0\mu} + S_\mu}{T + S_\mu} \tag{13}$$

where $T_{0\mu}$ and μ_0 are reference values, and S_μ is an effective temperature named Sutherland constant. The thermal conductivity is also obtained by Sutherland's formula. The shear stress transport (SST) $k-\omega$ turbulence model with a solve-to-wall strategy is adopted to close the governing equations.

A second-order total variation diminishing (TVD) scheme based on Harten–Lax–van Leer–Contact (HLLC) Riemann solver is employed. The implicit dual-time step method is used for time advancement, with a time step size of 1e−06 s. The internal iterations up to 50 steps for a single time step are set to reduce the residual error to below 1e–05. The numerical method used in this work is the same as that in existing studies [23,38], and it is verified using experimental results of SWBLI and moving shock wave [38,39].

B. Grid Convergence

To assess the grid dependence, four grids with different cell numbers N_{cell} are generated. The L_c and h_c are 25.4 and 17.78 mm, respectively. The contraction angles θ_c are 11° and 6°, and the initial flowfields are started and unstarted, respectively. The region where shock waves exist (x = 220–400 mm, y = 0–33 mm) is mainly refined with the first cell height fixed at 0.001 m, and the equivalent cell size h_{ce} is obtained within this region. The h_{ce} of the densest grid is about 1/100 of the entrance boundary-layer thickness. Table 2 lists the grid characteristics.

The SWBLI flowfields are simulated using these grids at the No. 1 flow condition, and the pressure distributions on the lower wall are compared in Fig. 4a. The pressure curves of different grids well coincide for both the started and unstarted states. Regarding the results of the densest grid as a benchmark, the relative errors of wall pressure peaks are calculated. Figure 4b illustrates the relative errors

Table 2 Grid characteristics and calculated wall pressure peak

Grid	N_{cell}, 10^6	h_{ce}, mm	δ_c/h_{ce}	$p_{\mathrm{max\text{-}st}}$, kPa	$p_{\mathrm{max\text{-}un}}$, kPa
Coarse	0.66	0.141	34.2	66.301	78.084
Moderate	1.2	0.094	51.3	65.988	77.213
Refined	2.3	0.068	70.9	65.789	76.659
Dense	4.0	0.051	94.5	65.595	76.304

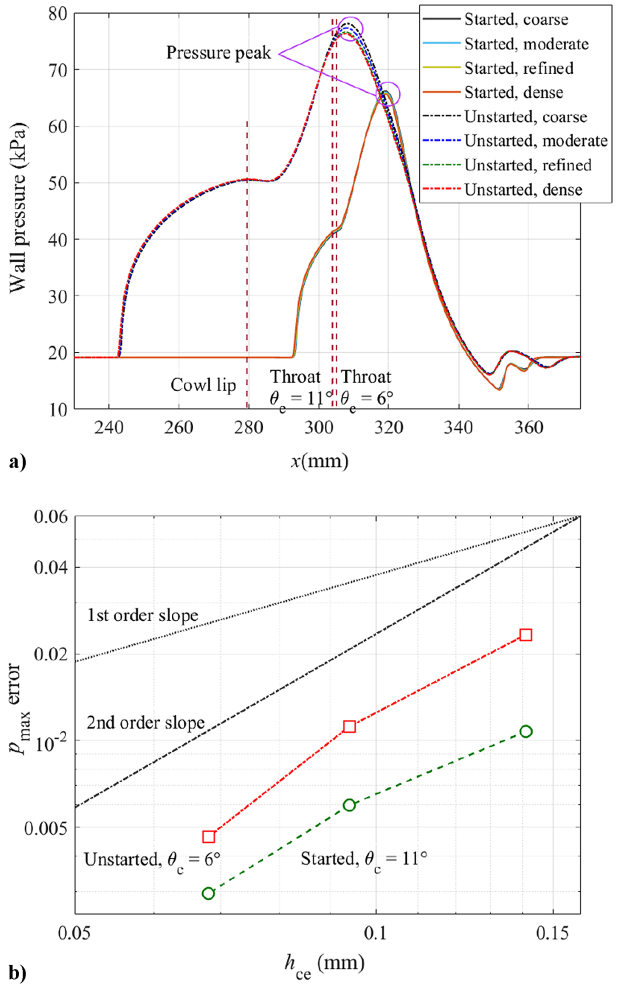

Fig. 4 Grid convergence analysis: a) wall pressure distribution; b) errors of wall pressure peak varying with characteristic cell size.

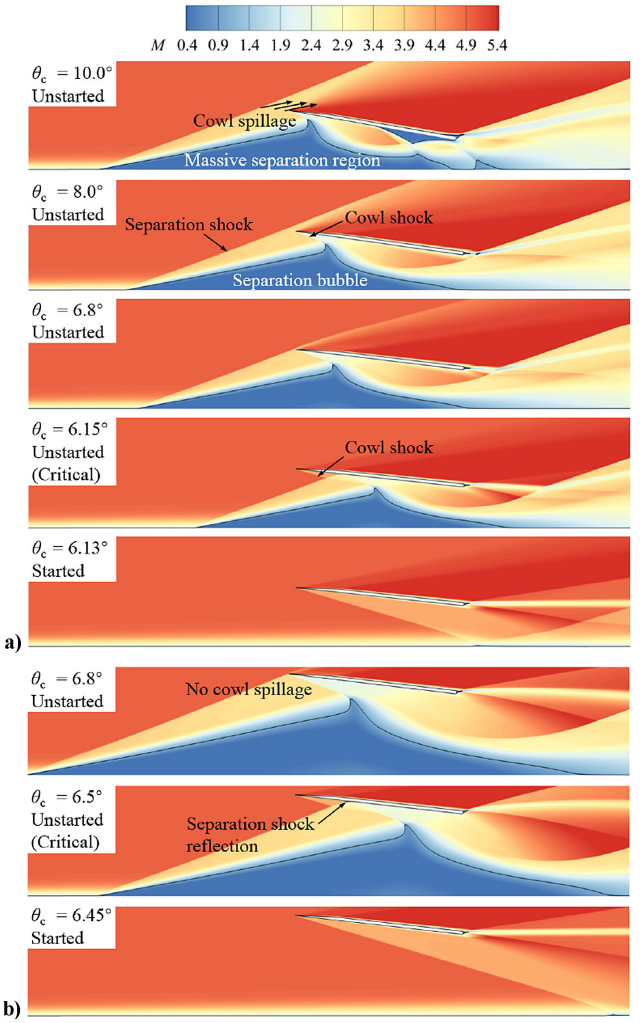

Fig. 5 Determination of restart boundary ($M_\infty = 5$, $L_c = 50.8$ mm, black lines show sonic location): a) $h_c = 17.78$ mm; b) $h_c = 30.48$ mm.

of pressure peaks $p_{max\text{-}st}$ and $p_{max\text{-}un}$ varying with h_{ce}. The errors are within 3% and converge with second order, which matches the design order of the spatial discretization scheme. The moderate grid is chosen to ensure the accuracy and save computing resources.

C. Determination of Restart Boundary

Utilizing the overset grid method, the cowl is rotated with a quasi-steady strategy to determine the restart boundary. The grid consists of two parts: the cowl grid and the background grid. At the initial stage, the throat height h_t is sufficiently small to ensure that the inlet is unstarted initially. For a given contraction angle, calculations are conducted until convergence, and the flowfield is saved. Subsequently, a new grid with a smaller contraction angle is generated to replace the existing grid. Iterations are then carried out for adequate time steps based on the saved flowfield. This process continues until the massive separation region disappears. The corresponding contraction angle is denoted as θ_{re}, i.e., the restart boundary, and the unstarted flowfield with a θ_c very close to θ_{re} is defined as the critical state.

Figure 5 illustrates the determination of the restart boundary. In the unstarted state, as the contraction angle decreases, the separation region on the upper surface disappears first, and the cowl lip spillage reduces because of the shrinking of the separation bubble. In Fig. 5a, the separation shock nearly intersects with the cowl lip at $\theta_c = 6.8°$, and the restart occurs at $\theta_c = 6.13°$. After the restart boundary is obtained at a given entrance height h_c, the other case groups of different h_c are conducted with the same L_c, for instance, $h_c =$ 30.48 mm (Fig. 5b). In Fig. 5b, the separation shock impinges downstream of the cowl lip at $\theta_c = 6.8°$, the restart occurs at $\theta_c = 6.45°$.

A comparison of Figs. 5a and 5b reveals that the higher cowl lip precipitates the occurrence of restart. The reason is that the separation scale is proportional to the characteristic boundary-layer displacement thickness, δ_c^* [20,25]. For a given L_f, if the incident shock waves have the same deflection angle θ_c (i.e., the same shock intensity) but different initiation points, the separation scale relative to the entry height will decrease as h_c increases. Hence, at a larger h_c, the separation bubble will earlier reach the position where a mismatch occurs between the intensity of the cowl shock system and the separation scale [23], resulting in a restart.

III. Extended Similarity Law for Restart Boundaries

A. Restart Boundaries Represented by Contraction Angle

1. *Specific Similarity Law*

The restart boundaries under different Mach numbers as functions of cowl length are displayed in Fig. 6. The restart phenomenon is influenced by multiple geometric and aerodynamic factors. For shorter cowls, higher entrances, higher static pressure, or incoming Mach numbers, the restart is more likely, and larger θ_{re} are achieved. The data tendency is consistent with the experimental results [5,25]. For each h_c, the drop-plateau-drop trend of θ_{re} caused by the increasing L_c is attributed to the relative length relationship between the cowl and the separation region [23]. With L_c fixed, the discrete distribution of θ_{re} is caused by the relative entrance height, as illustrated in Fig. 5.

To describe the effects of multiple factors in a unified formula, the abscissa of Fig. 6 is replaced by L_c^* utilizing Eq. (5). In Fig. 7a, the data points of different Mach numbers fall onto four curves,

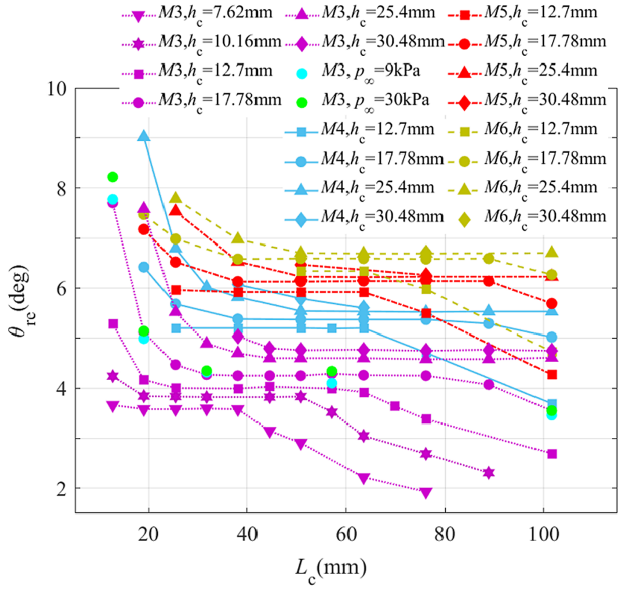

Fig. 6 Restart boundaries varying with Mach number.

respectively, and θ_{re} presents a drop-plateau-drop trend as L_c^* increases for each curve. The plateau contraction angle for restart $\theta_{re\text{-}pl}$ is extracted and shown in Fig. 7b, indicating an increasing trend with the relative cowl lip height h_c/δ_c^* and Mach number.

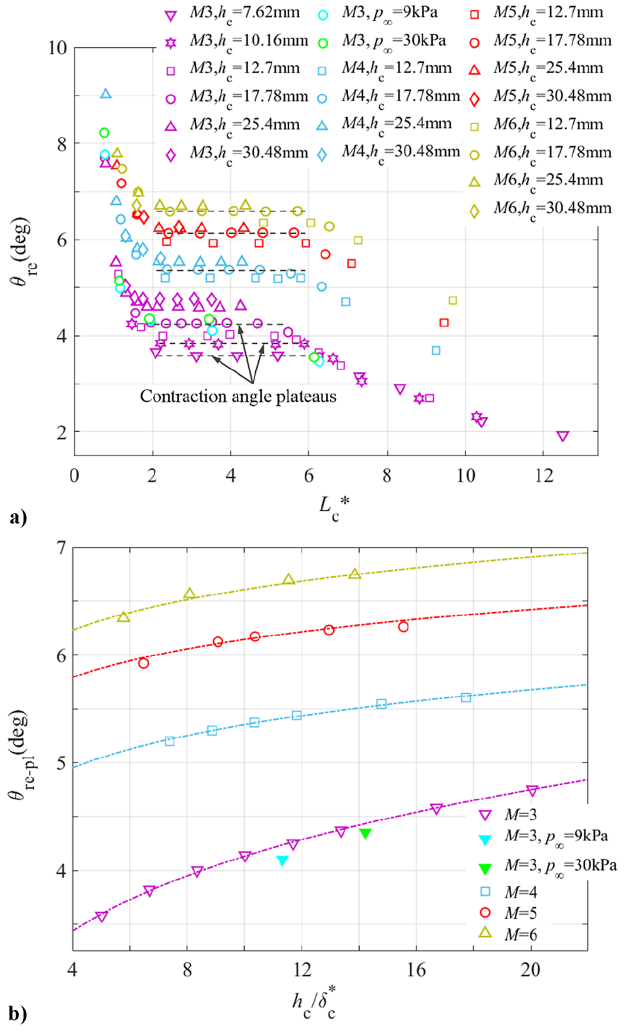

Fig. 7 Data collapse in restart boundaries: a) restart contraction angles; b) plateau angles.

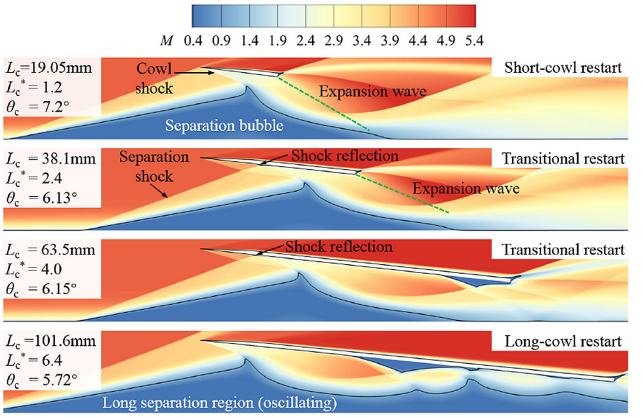

Fig. 8 Typical critical flowfields of different restart modes ($M_\infty = 5$, green dashed line shows the first expansion wave from the cowl tail).

Though data collapse is achieved using these dimensionless parameters, the data of the same L_c^* or h_c/δ_c^* but different Mach numbers remains discrete, indicating that the existing similarity law is specific rather than universal.

The critical flowfields of the three restart modes are shown in Fig. 8, corresponding to the three segments of curves in Fig. 7a. In the critical states of short-cowl and transitional modes, a massive separation bubble stands at the entrance of the duct. The separation bubble of short-cowl mode is affected by the expansion waves from the cowl tail, and there is competition between the incident cowl shock and the trailing expansion waves. For the transitional mode, the separation bubble is sustained by the cowl shock wave and the reflected separation wave together, but it is decoupled from the expansion waves. Hence, the restart contraction angle is independent of the cowl length and throat height. For the long-cowl restart, the long separation region is sustained by the throat flow choke and the cowl shock wave together. The detailed critical flow structures and unsteady processes of the three restart modes are analyzed in our previous study [23].

2. *Generalized Similarity Law*

The similarity of the restart boundary stems from the critical flowfields. Taking the short-cowl restart as an example, the mechanism is discussed as follows. Figure 9 illustrates the flowfields near the restart boundary with $L_c^* \approx 1.6$. At $M_\infty = 6$, for the given L_c^*, the position and scale of the unstarted separation bubble relative to the duct entrance remain unchanged in the critical state (Figs. 9a and 9c), regardless of the entrance height h_c. Thus, geometric similarity is satisfied. The influence mechanism of h_c can also be explained based on Figs. 9a and 9c. In the critical state, if h_c increases with θ_c fixed, the impingement position of the trailing expansion waves will move upstream and destabilize the separation region. Consequently, a longer cowl plate is required to keep the expansion waves distant from the leeward surface of the separation region, and the massive separation region is sustained.

On the other hand, with L_c^* fixed, the restart contraction angle θ_{re} is smaller at Mach 3 (Figs. 9f and 9g); the reason is that at the same θ_c, both the cowl shock angle β_2 and the separation shock angle β_s increase as the Mach number decreases. This makes the apex of the large separation region located further upstream and more difficult to recede at low Mach numbers (Fig. 9e shows that cowl spillage still exists at Mach 3, $\theta_c = 7°$), thereby necessitating a further reduction in θ_c to achieve restart. This leads to the question of whether there is a similarity relationship between critical contraction angles at different Mach numbers. The stabilization mechanism of the critical separation bubble involves the relative separation scale to the contraction duct, as well as the competition between the cowl shock system and the trailing expansion waves. Given the difficulty in predicting the restart phenomenon using first-principles analysis, similarity analysis methods are considered to simplify the problem.

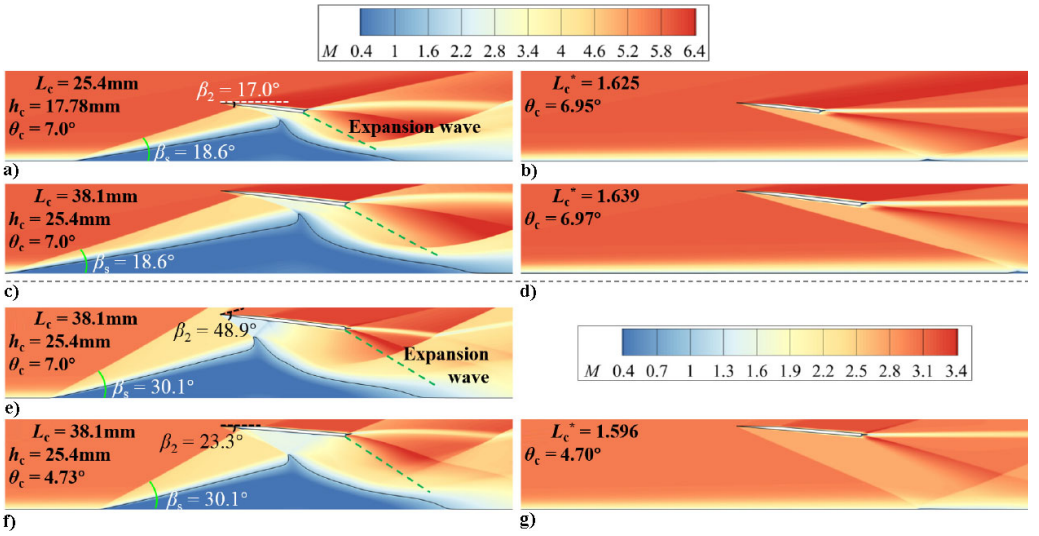

Fig. 9 Similarity in critical flowfields (black lines show sonic location): a–d) $M_\infty = 6.0$; e–g) $M_\infty = 3.0$.

Similarity theory indicates that self-similar solutions can be divided into two categories [40,41]. Self-similar solutions obtained through dimensional analysis belong to the self-similarity of the first kind, with similarity relationships expressed as $\Pi = \Phi(\theta)$. The self-similarity of the second kind, referred to as nontrivial, cannot be fully determined by dimensional analysis alone. Its similarity relationship takes the form $\Pi/\eta^\alpha = \Phi(\xi/\eta^\kappa)$, and it can be further categorized into Class A and Class B based on whether the exponents are constant.

Returning to the existing specific similarity laws, the restart contraction angles are functions of the dimensionless cowl length:

$$\begin{aligned} \theta_{\mathrm{re}} &= f_1(L_c^*), \quad M_\infty = M_1; \\ \theta_{\mathrm{re}} &= f_2(L_c^*), \quad M_\infty = M_2; \ \ldots \end{aligned} \tag{14}$$

The functions $f_1, f_2, \ldots$ have similar forms at each Mach number, and the influence of Reynolds number is incorporated into L_c^* through δ_c^*. Therefore, the restart boundary may possess a higher level of symmetry, enabling data collapse in a wider range. A trial power function about M_∞ can be used to construct a new similarity parameter:

$$\theta_{\mathrm{reM}} = \frac{\theta_{\mathrm{re}}}{M_\infty^\alpha} = \Phi\left(L_c^* \ \text{ or } \ \frac{h_c}{\delta_c^*}\right) \tag{15}$$

in which θ_{reM} is the modified contraction angle. If the self-similarity of the second kind exists, the function Φ will remain invariant at different Mach numbers, so that θ_{reM} can be a univariate function of L_c^* or h_c/δ_c^*.

Based on the numerical results, the exponent α is sought by empirical attempts. Certainly, a data-driven neural network [41] can also be used. It is found that α depends on the restart modes or L_c^*:

$$\alpha = \begin{cases} 0.6, & L_c^* < 2 \\ 0.75, & 2 < L_c^* < 6 \\ 0.9, & L_c^* > 6 \end{cases} \tag{16}$$

The invariance of Φ is then examined under the given α. The ordinate of Fig. 6 is replaced by θ_{reM}, as shown in Fig. 7. The three sections of the curve with different slopes denote three restart modes. For $L_c^* < 2.0$ and $L_c^* > 6.0$, the data points fall onto the same curve (Fig. 10a), i.e., θ_{reM} is a single-variable function of L_c^*. For $2.0 < L_c^* < 6.0$, the plateau angle $\theta_{\text{re-plM}}$ is a single-variable function of h_c/δ_c^* (Fig. 10b).

Figure 10 confirms that the effect of M_∞ is decoupled from L_c^* and h_c/δ_c^*, and hence a unified fitting equation is established:

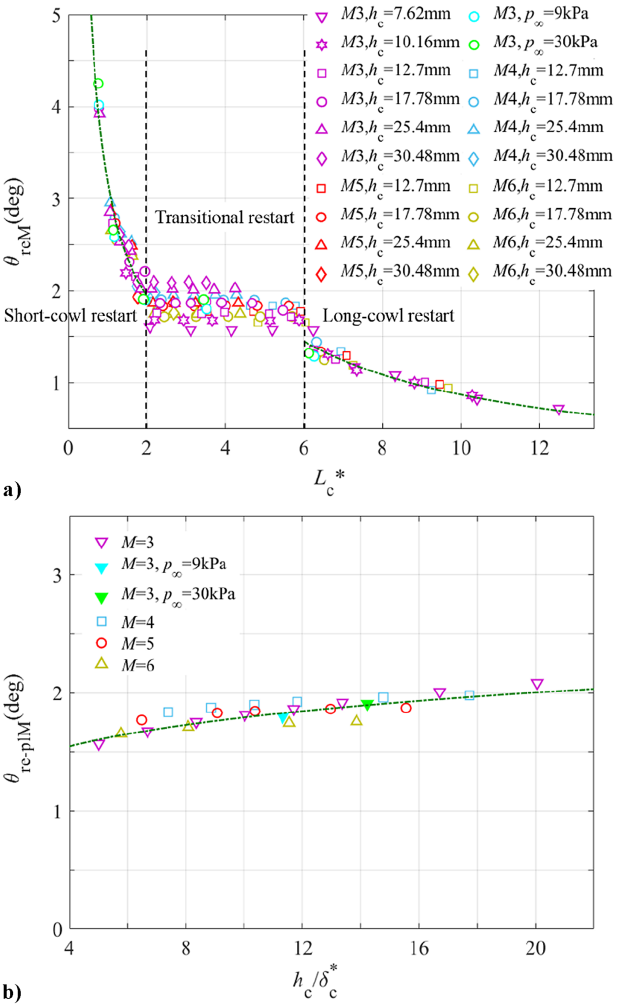

Fig. 10 Modified similarity law and fitting curve: a) restart contraction angles; b) plateau angles.

$$\theta_{\mathrm{reM}} = \begin{cases} \dfrac{2.5}{L_c^*} + 0.7, & L_c^* < 2 \\ 1.24\left(\dfrac{h_c}{\delta_c^*}\right)^{0.16}, & 2 < L_c^* < 6 \\ \dfrac{8.7}{L_c^*}, & L_c^* > 6 \end{cases} \tag{17}$$

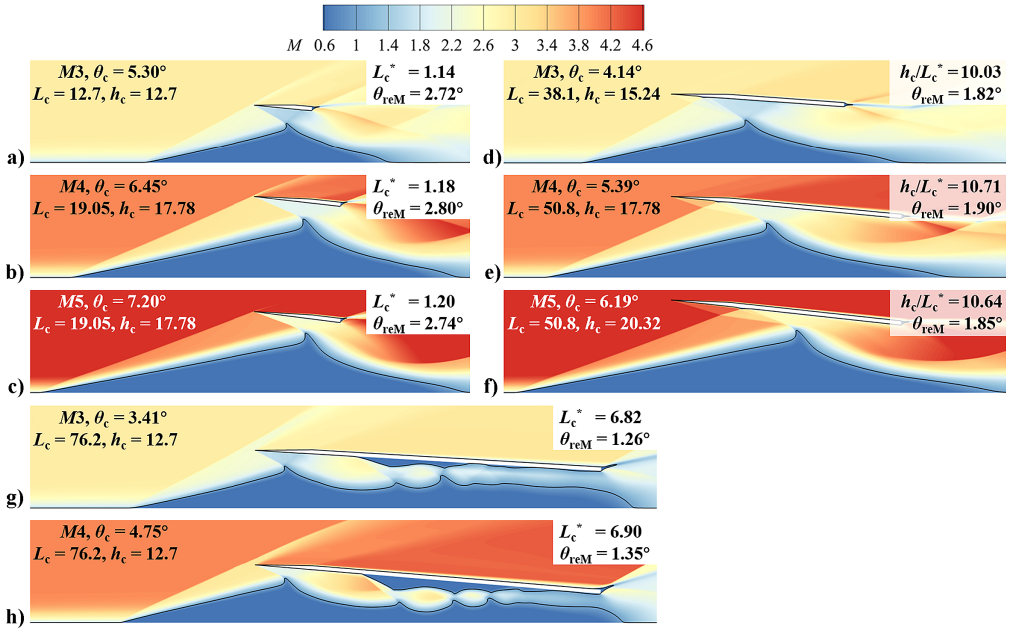

Fig. 11 Critical flowfields of the generalized similarity (length dimension in mm): a–c) short-cowl restart, $\theta_{re} = 5.25°$, 6.40°, and 7.15°; d–f) transitional restart, $\theta_{re} = 4.13°$, 5.37°, and 6.17°; g–h) long-cowl restart, $\theta_{re} = 3.38°$ and 4.71°.

The curve of Eq. (17) closely matches the data points. According to the data in Fig. 10, typical critical flowfields of the three restart modes are selected, as shown in Fig. 11. Figures 11a–11c belong to the short-cowl restart. Fixing L_c^* around 1.17 with a variation of ±2.6%, the corrected contraction angle for restart, θ_{reM}, remains at 2.76° ± 1.4% regardless of the entrance Mach number. The critical flowfields of transitional restart (Figs. 11d–11f) show a couple of invariable parameters: $h_c/\delta_c^* = 10.37 \pm 3.3\%$, and $\theta_{\mathrm{reM}} = 1.86° \pm 2.1\%$. Hence, they exhibit a form of generalized similarity at the same $(h_c/\delta_c^*, \theta_{\mathrm{reM}})$ regardless of M_∞ and L_c/δ_c^*. The long-cowl restart (Figs. 11g and 11h) also obeys the similarity relationship based on $(L_i^*, \theta_{\mathrm{reM}})$. It is worth noting that the similarity relationship is valid only for the same restart mode; there is no similarity relationship between the critical flowfields of different restart modes.

B. Restart Boundaries Represented by Internal Contraction Ratio

Compared to the cowl length, ICR is more commonly used in the inlet design. Hence, the self-similar form of ICR is explored. In Fig. 12a, the existing effective throat-entrance area ratio [Eq. (6)] keeps self-similar only at specific Mach numbers. To overcome this shortcoming, a corrected area ratio can be defined based on θ_{reM}:

$$\mathrm{ICR}_{\mathrm{eff\text{-}reM}}^{-1} = 1 - L_c^* \sin\left(\frac{\theta_{\mathrm{re}}}{M^{\alpha}}\right) \tag{18}$$

Figure 12b illustrates the data processed by the corrected area ratio, where the θ_{reM} of the transitional restart is fixed at 1.75° for simplicity. The data points converge to a single curve with a relative error within 5%.

Thus, the extended similarity law has achieved a unified description of Mach number effects. Previous studies in the traditional theoretical framework has been dedicated to establishing a functional relation between the area ratio and Mach number. However, the self-similar function obtained in this paper is independent of the Mach number, indicating an inherent geometric similarity law for the restart phenomenon. Its physical mechanism, rooted in SWBLI, needs further study.

Considering the compatibility of ICR and $\mathrm{ICR}_{\mathrm{eff}}$, a conversion method for the corrected contraction ratio $\mathrm{ICR}_{\mathrm{effM}}$ is provided.

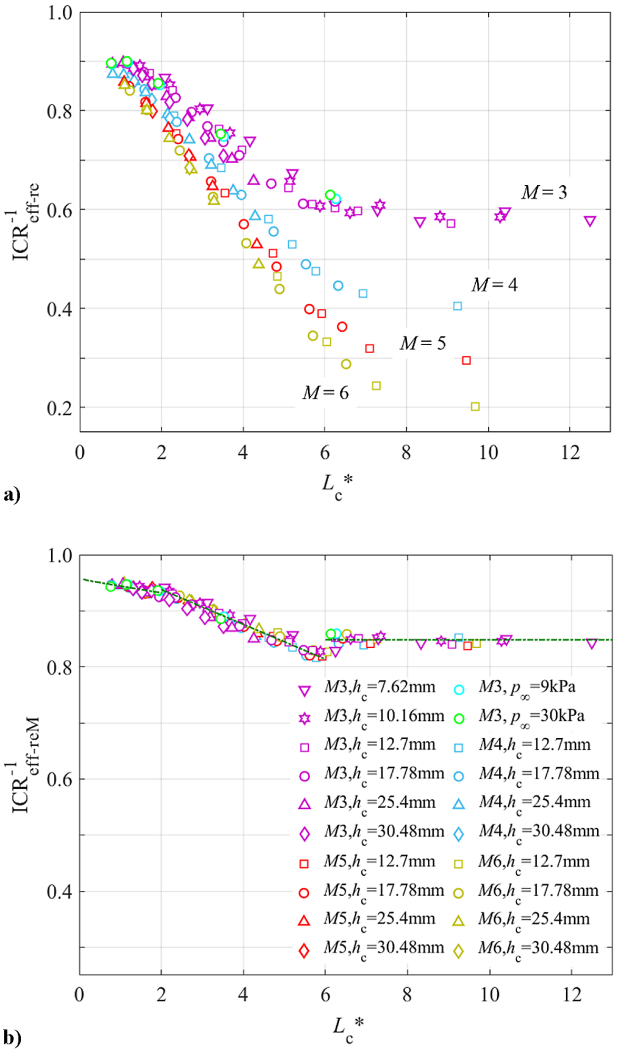

Fig. 12 Restart boundaries represented by area ratio: a) effective area ratio; b) corrected area ratio.

Firstly, the $\mathrm{ICR}_{\mathrm{eff}}$ is yielded from the traditional ICR and relative entrance height h_c/δ_c^*:

$$\mathrm{ICR}_{\mathrm{eff}}^{-1} = \frac{\mathrm{ICR}^{-1} - \delta_c^*/h_c}{1 - \delta_c^*/h_c} \tag{19}$$

Then using $\sin(\theta_c/M^\alpha) \approx \theta_c/M^\alpha$, the $\mathrm{ICR}_{\mathrm{effM}}$ is obtained:

$$\mathrm{ICR}_{\mathrm{effM}}^{-1} \approx 1 - \frac{1}{M^\alpha} + \frac{1}{M^\alpha}(1 - L_c^*\theta_c) = 1 - \frac{1}{M^\alpha}(1 - \mathrm{ICR}_{\mathrm{eff}}^{-1}) \tag{20}$$

The restart boundaries in the literature are extracted and processed by Eqs. (19) and (20) to further validate the extended similarity law. The experimental [4,5,10,24,25] and numerical results [9,21,26–33] are listed in Tables 3 and 4, respectively. The necessary geometric and aerodynamic parameters are supplemented according to the literature.

The corrected area ratios in Tables 3 and 4 are illustrated in Fig. 13. The abscissa is the corrected contraction angle θ_{cM} as it is easier to determine θ_{cM} rather than L_c^* in engineering. Figure 13 indicates that the corrected area ratio lies between 0.8 and 0.92, and most data points belong to the short-cowl unstart. It is worthy to note that the $\mathrm{ICR}_{\mathrm{effM}}$ of the transitional restart increases suddenly within $\theta_{\mathrm{cM}} = 1.5° \sim 2.4°$.

An empirical equation can be established by representing L_c^* as an inverse function of θ_{reM} [Eq. (17)] and substituting it into Eq. (18). This formula has a relative error within 10% for the simplified inlets without an expansion corner, while the maximum error for the inlets with an expansion corner is about 19% (the data points in the ellipse). The reason is that two-dimensional numerical simulation tends to give a conservative prediction of restart boundaries compared to experiments [25], and the expansion corner reduces the pressure downstream of the separation region and facilitates the restart [42]. Therefore, the parameters in the current formula are modified for three kinds of inlets:

Table 3 Restart boundaries obtained by experiments [4,5,10,24,25]

Ref.	M_∞	θ_c, deg	α	θ_{cM}, deg	h_c, mm	ICR^{-1}	δ_c^*, mm	$\mathrm{ICR}_{\mathrm{eff}}^{-1}$	$\mathrm{ICR}_{\mathrm{effM}}^{-1}$
Emami 1995 [4]	3.22	4.5	0.75	1.872	15.14	0.671	0.914	0.650	0.854
	3.22	3.0	0.9	1.047	15.34	0.662	0.914	0.641	0.874
	3.22	2.9	0.9	1.012	15.81	0.642	0.914	0.620	0.867
	3.22	3.7	0.75	1.539	14.26	0.712	1.854	0.669	0.862
	3.22	2.7	0.6	0.943	14.83	0.685	1.854	0.640	0.874
	3.22	2.3	0.6	0.803	14.65	0.695	1.854	0.649	0.878
Van Wie 1996 [5]	2.9	11	0.6	5.807	17.78	0.796	1.51	0.777	0.882
	2.9	8.6	0.6	4.540	17.78	0.786	1.51	0.767	0.877
	2.9	6.2	0.75	2.790	17.78	0.769	1.51	0.747	0.883
	2.9	8.7	0.6	4.593	12.7	0.773	1.51	0.742	0.864
	2.9	6.2	0.6	3.273	12.7	0.784	1.51	0.755	0.871
	2.9	5.5	0.75	2.475	12.7	0.712	1.51	0.674	0.853
	2.9	4.0	0.9	1.534	7.62	0.767	1.51	0.710	0.889
	2.9	10.3	0.6	5.437	17.78	0.808	1.76	0.787	0.888
	2.9	5.4	0.9	2.071	17.78	0.798	1.76	0.776	0.914
	2.9	5.6	0.75	2.520	12.7	0.804	1.76	0.773	0.898
	2.9	4.7	0.75	1.803	12.7	0.713	1.76	0.667	0.872
Li 2012 [24]	4.0	14.0	0.6	6.094	28.57	0.657	1.97	0.632	0.840
Yue 2018 [25]	3.9	9.0	0.6	3.977	40	0.741	2.6	0.723	0.875
	3.9	11.0	0.6	4.861	40	0.833	2.6	0.821	0.921
	3.9	15.0	0.6	6.629	40	0.8	2.6	0.786	0.905
	3.9	7.0	0.9	2.057	20	0.667	3.45	0.597	0.882
	3.9	7.0	0.9	2.057	20	0.781	4.13	0.724	0.919
	3.9	7.0	0.9	2.057	30	0.571	3.8	0.509	0.856
	3.9	9.0	0.6	3.977	30	0.833	3.8	0.809	0.915
	5.9	7.0	0.9	1.417	20	0.410	2.42	0.328	0.864
	5.9	15.0	0.6	5.171	20	0.741	2.42	0.705	0.898
	5.9	9.0	0.75	2.377	20	0.595	4.4	0.481	0.863
	5.9	11.0	0.6	3.792	20	0.781	4.4	0.719	0.904
	5.9	13.0	0.6	4.482	20	0.769	4.4	0.704	0.898
Jin 2023 [10]	2.47	8.0	0.75	4.060	24.16	0.676	0.72	0.666	0.830

Table 4 Restart boundaries obtained by numerical simulation [9,21,26–33]

Ref.	M_∞	θ_c, deg	α	θ_{cM}, deg	h_c, mm	ICR^{-1}	δ_c^*, mm	$\mathrm{ICR}_{\mathrm{eff}}^{-1}$	$\mathrm{ICR}_{\mathrm{effM}}^{-1}$
Chang 2009 [26]	2.68	10.0	0.6	5.535	19.36	0.723	2.55	0.681	0.823
Fan 2009 [27]	2.99	7.0	0.75	3.077	17.05	0.645	2.66	0.579	0.815
You 2011 [28]	3.34	8.6	0.6	4.171	74.4	0.833	7.5	0.814	0.910
	5.82	8.6	0.6	2.989	74.4	0.625	8.3	0.578	0.853
	6.57	8.6	0.75	2.096	74.4	0.5	8.9	0.432	0.862
Li 2016 [29]	3.47	14.0	0.6	6.635	15.30	0.654	1.76	0.608	0.814
Guo 2017 [30]	4.25	14.0	0.6	5.874	17.70	0.565	1.85	0.515	0.796
Su 2017 [31]	3.57	9.0	0.6	4.195	21.30	0.704	1.83	0.676	0.849
Xie 2020 [32]	3.76	8.0	0.6	3.616	17.06	0.668	3.25	0.590	0.815
Reardon 2021 [9]	3.22	3.0	0.9	1.047	16.01	0.635	0.88	0.613	0.865
Jin 2022 [33]	2.42	10.0	0.6	5.884	74.9	0.763	1.49	0.758	0.858
	3.0	10.0	0.6	5.173	74.9	0.8	1.68	0.795	0.894
Yang 2024 [21]	2.58	13.8	0.6	7.815	24.0	0.714	2.74	0.677	0.817
	2.94	12.8	0.6	6.702	24.0	0.714	3.05	0.672	0.828
	3.77	10.8	0.6	4.871	24.0	0.714	3.05	0.667	0.850

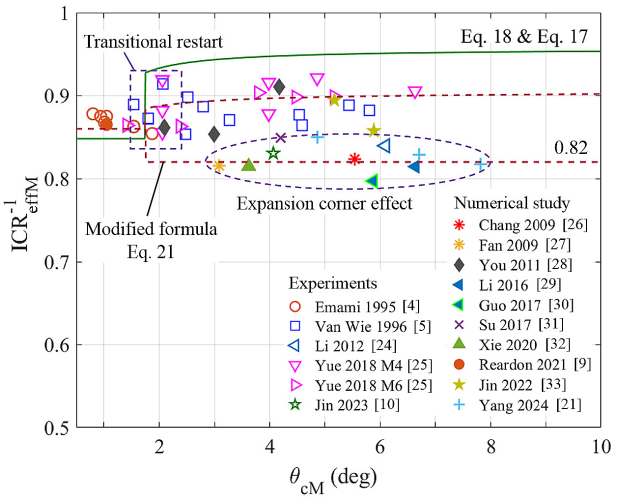

Fig. 13 Empirical formula of corrected area ratio for restart comparing with literature data [4,5,9,10,21,24–33].

$$\mathrm{ICR}_{\mathrm{effM}}^{-1}=\begin{cases}0.86, & \theta_{\mathrm{cM}}<1.75\\ 1-\dfrac{5.5}{\theta_{\mathrm{cM}}-0.3}\sin\theta_{\mathrm{cM}}, & \theta_{\mathrm{cM}}>1.75\\ 0.82, & \theta_{\mathrm{cM}}>1.75,\ \text{Expansion corner}\end{cases} \tag{21}$$

For the inlets with an expansion corner, the corrected area ratio of 0.82 is taken as the restart boundary, while the expansion corner effect is negligible for small contraction angles. The modified empirical equation has an error within 5%. In contrast, Kantrowitz and Sun's equations show errors up to 33 and 43%, respectively (Fig. 1).

IV. Wall Pressure Characteristics of Restart Phenomenon

In the flight tests of hypersonic air-breathing propulsion, the wall pressure signal is the main criterion for the operation state of the inlets [3]. Therefore, the critical wall pressure curves are analyzed to explore the similarity law at variable Mach numbers. The wall pressure distributions of various configurations at a fixed Mach number are displayed in Fig. 14a. For each curve, the upstream pressure step corresponds to the initiation of the separation shock, and the pressure peak $p_{\max}$ occurs downstream of the separation region. For different Mach numbers, the dimensionless streamwise pressure difference $p_{\max}/p_{\infty}-1$ is extracted, which is related to the separation scale. Figure 14b indicates that the pressure difference in the critical state increases with Mach number and L_c^* in a discrete form.

The previous study proposed a self-similar dimensionless pressure rise at specific Mach numbers [38] based on the correlation between the characteristic separation length and the pressure difference [43]. The expression is

$$p_{\mathrm{rec}}^{*}=\left(\frac{p_{\max\text{-re}}}{p_{\infty}}-1\right)^{b}\frac{\delta_c^{*}}{h_c} \tag{22}$$

Here b is an empirical parameter that can be fitted by a function of Mach number according to the data in Fig. 10b:

$$b=2.77+0.2\times0.5^{M_{\infty}-3} \tag{23}$$

In Fig. 15, p_{rec}^{*} still illustrates a discrete distribution for different Mach numbers. Because the separation scale is mainly decided by the cowl shock strength, the pressure rise of the cowl shock can be incorporated in the p_{rec}^{*}, and a new similarity quantity p_{recM}^{*} can be constructed:

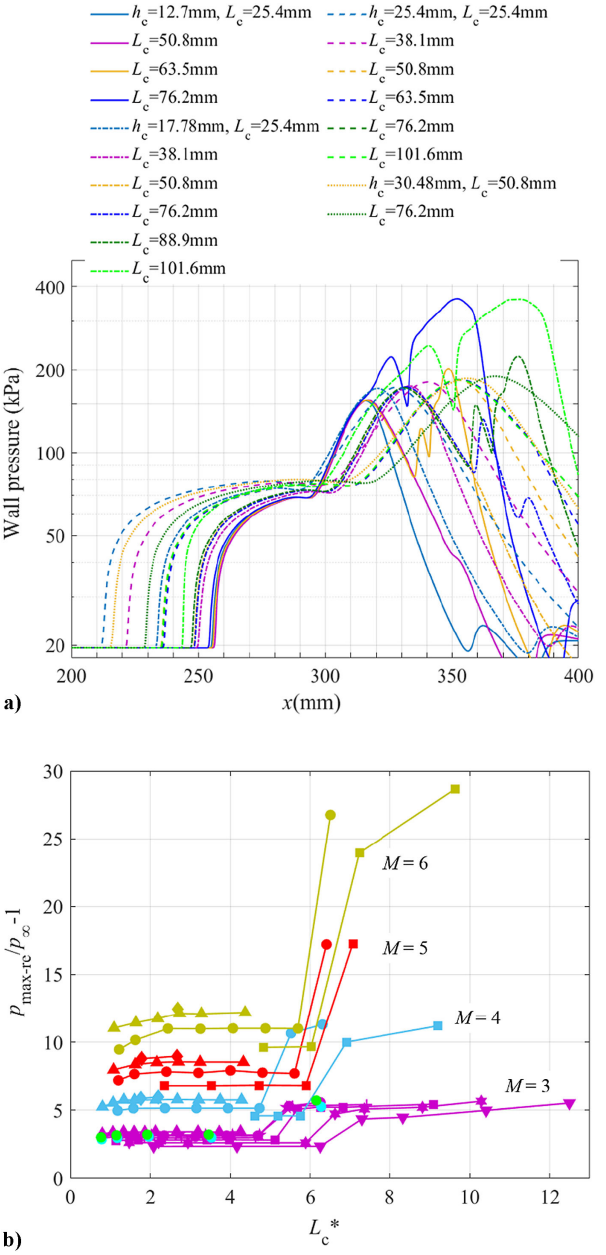

Fig. 14 Critical wall pressure characteristics: a) wall pressure distribution varying with contraction angle and entrance height ($M_{\infty}=5$); b) dimensionless streamwise pressure difference.

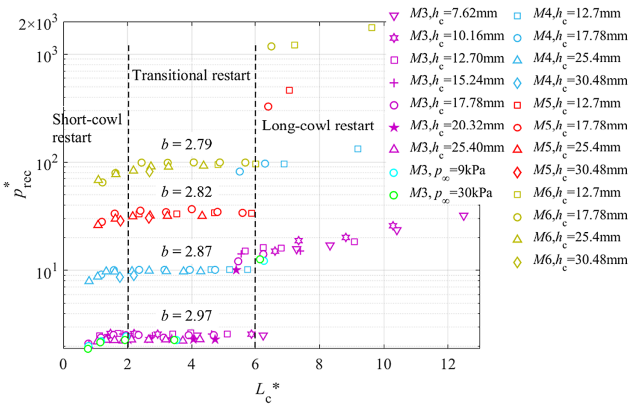

Fig. 15 Similarity law of critical pressure rise at specific Mach numbers.

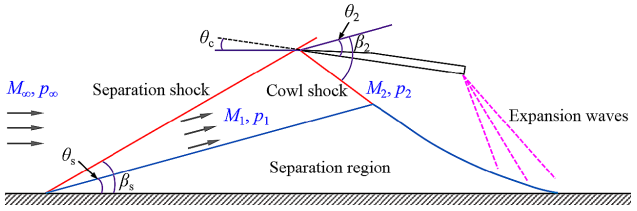

Fig. 16 Schematic shock wave system at the entrance in critical state.

$$p^*_{\mathrm{recM}} = f\left(\frac{p_{\max\text{-re}}}{p_\infty}, \frac{\delta^*_c}{h_c}, \frac{p_2}{p_1}\right) \tag{24}$$

The p_1 and p_2 are the static pressures before and behind the cowl shock, respectively.

The p_2/p_1 is calculated according to the critical flow structure shown in Fig. 16. For brevity, the short-cowl restart is analyzed, and the other two modes share the same method. First, the flow parameters behind the separation shock are obtained by the free interaction theory [44]. The separation shock angle depends on the incoming Mach number:

$$\beta_s = \arcsin\sqrt{\frac{1}{M^2_\infty} + C_f\frac{\gamma+1}{(M^2_\infty-1)^{0.25}}} \tag{25}$$

Here C_f is the coefficient of wall friction [42]. Then the separation wedge angle θ_s and the Mach number behind the separation shock M_1 are yielded by the oblique shock relation:

$$\tan\theta_s = 2\cot\beta_s\frac{M^2_\infty\sin^2\beta_s - 1}{M^2_\infty(\gamma+\cos 2\beta_s)+2} \tag{26}$$

$$M^2_1 = \frac{M^2_\infty + \frac{2}{\gamma-1}}{\frac{2\gamma}{\gamma-1}(M_\infty\sin\beta_s)^2 - 1} + \frac{(M_\infty\cos\beta_s)^2}{\frac{\gamma-1}{2}(M_\infty\sin\beta_s)^2 + 1} \tag{27}$$

The flow deflection angle is the sum of the contraction angle and the separation angle:

$$\theta_2 = \theta_c + \theta_s \tag{28}$$

Employing Eqs. (26) and (27) once again with M_1 and θ_2 gives the cowl shock angle β_2, and the pressure ratio is

$$\frac{p_2}{p_1} = 1 + \frac{2\gamma}{\gamma+1}\left[(M_1\sin\beta_2)^2 - 1\right] \tag{29}$$

The similarity quantity p^*_{recM} can be constructed by adding a power function of $p_2/p_1 - 1$ to Eq. (22):

$$p^*_{\mathrm{recM}} = \frac{\delta^*_c}{h_c}\frac{(p_{\max\text{-re}}/p_\infty - 1)^b}{(p_2/p_1 - 1)^d} \tag{30}$$

Here d is an empirical parameter depending on the restart mode according to the numerical results:

$$d = \begin{cases} 3.0, & L^*_c < 2 \\ 3.2, & 2 < L^*_c < 6 \\ 3.9, & L^*_c > 6 \end{cases} \tag{31}$$

The pressure rise reprocessed by p^*_{recM} is illustrated in Fig. 17, in which the data points converge to a three-segment curve (green dash-dot line). Generally, p^*_{recM} is a function of L^*_c only:

$$p^*_{\mathrm{recM}} = \begin{cases} (L^*_c - 0.7)^{0.4} - 0.1, & L^*_c < 2 \\ 0.85, & 2 < L^*_c < 6 \\ 2.2L^*_c - 9, & L^*_c > 6 \end{cases} \tag{32}$$

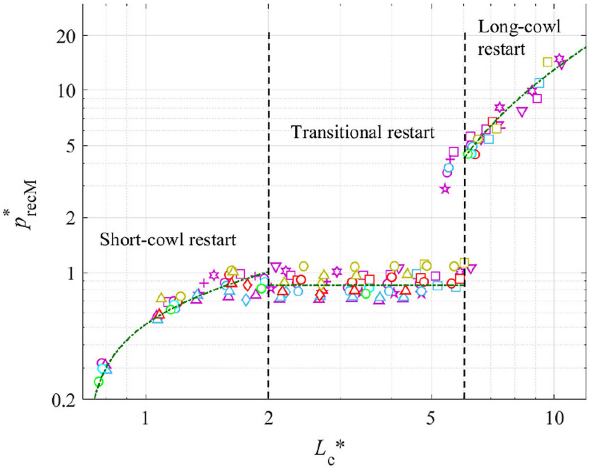

Fig. 17 Unified similarity law for restart-critical wall pressure rise (the symbol legend is the same as in Fig. 12).

The practical inlets usually belong to the short-cowl restart ($L^*_c < 2$). Note that the p^*_{recM} of the transitional restart ($2 < L^*_c < 6$) presents a plateau because the characteristic separation scale is proportional to the effective entrance height but independent of the cowl length. The curve of long-cowl restart ($L^*_c > 6$) is the steepest as a result of the shock wave reflection in the duct.

The error of the fitting curve is within 15% except in the region near the switching point. The current empirical formula can be a supplementary criterion for inlet operation state, and the accuracy can be improved by introducing detailed theoretical models of the critical separation scale.

V. Conclusions

To develop a universal prediction method for restart phenomenon of hypersonic inlets, two-dimensional RANS numerical simulation on simplified contraction ducts is conducted. The restart is implemented by rotating the cowl anticlockwise around the cowl lip, and the similarity in restart boundaries at variable Mach numbers is explored.

The similarity of the restart boundary stems from the critical flowfields. When exploring the restart similarity law and constructing similarity parameters, the assumption of the second kind of self-similarity is adopted. By proposing the corrected contraction angle and contraction ratio, this paper extends the existing similarity law for hypersonic inlet restart to variable Mach numbers. The complete statement of the similarity law is as follows: if two contraction ducts share the same (θ_{cM}, L^*_c), or (θ_{cM}, $\mathrm{ICR}_{\mathrm{effM}}$), or ($L^*_c$, $\mathrm{ICR}_{\mathrm{effM}}$), their restart characteristics are identical. The empirical equation based on the extended similarity law shows a maximum deviation of 5% from the literature data. For practical use, conversion formulas between the traditional ICR, effective ICR, and corrected ICR are given.

To facilitate restart detection in wind-tunnel and flight tests, a self-similar wall pressure criterion for restart, p^*_{recM}, is established by correlating the critical wall pressure rise with the cowl shock strength in the form of a power function. The corrected pressure criterion is a one-variable function of dimensionless cowl length, which can be used in the situations with varying Mach numbers. The physical implications of the similarity law may be explained with more profound theoretical tools of SWBLI in future studies. Moreover, the prediction method can be improved by considering the restart auxiliary means, such as expansion corners and boundary-layer bleeding.

Acknowledgment

This work is sponsored by the National Natural Science Foundation of China (Nos. 12402383, U2141220, 12372236, U2341240).

References

[1] Heiser, W. H., Pratt, D. T., Daley, H. D., and Mehta, U. B., *Hypersonic Airbreathing Propulsion*, AIAA, Washington, D.C., 1994, pp. 197–267.

[2] Van Wie, D. M., "Scramjet Inlets," *Scramjet Propulsion*, edited by P. Zarchan, Progress in Astronautics and Aeronautics, AIAA, Reston, VA, 2001, pp. 447–511.

[3] Chang, J. T., Li, N., Xu, K. J., Bao, W., and Yu, D. R., "Recent Research Progress on Unstart Mechanism, Detection and Control of Hypersonic Inlet," *Progress in Aerospace Sciences*, Vol. 89, 2017, pp. 1–22.
https://doi.org/10.1016/j.paerosci.2016.12.001

[4] Emami, S., Trexler, C. A., Auslender, A. H., and Weidner, J. P., "Experimental Investigation of Inlet-Combustor Isolators for a Dual-Mode Scramjet at a Mach Number of 4," NASA TP 3502, 1995.

[5] Van Wie, D. M., Kwok, F. T., and Walsh, R. F., "Starting Characteristics of Supersonic Inlets," AIAA Paper 1996-2914, July 1996.
https://doi.org/10.2514/6.1996-2914.

[6] Mayer, D. W., and Paynter, G. C., "Prediction of Supersonic Inlet Unstart Caused by Freestream Disturbances," *AIAA Journal*, Vol. 33, No. 2, 1995, pp. 266–275.
https://doi.org/10.2514/3.12418

[7] Teng, J., and Yuan, H. C., "Variable Geometry Cowl Sidewall for Improving Rectangular Hypersonic Inlet Performance," *Aerospace Science and Technology*, Vol. 42, 2015, pp. 128–135.
https://doi.org/10.1016/j.ast.2015.01.011

[8] Shi, W., Chang, J. T., Wang, Y. Y., Bao, W., and Liu, X. Y., "Buzz Evolution Process Investigation of a Two-Ramp Inlet with Translating Cowl," *Aerospace Science and Technology*, Vol. 84, 2019, pp. 712–723.
https://doi.org/10.1016/j.ast.2018.11.016

[9] Reardon, J. P., Schetz, J. A., and Todd Lowe, K., "Computational Analysis of Unstart in Variable-Geometry Inlet," *Journal of Propulsion and Power*, Vol. 37, No. 4, 2021, pp. 564–576.
https://doi.org/10.2514/1.B38214

[10] Jin, Y., Tan, H. J., Zhang, H., Zheng, G. J., Sun, S., and Zhang, Y., "Experimental Investigation on Unstart-Restart Hysteresis of a Supersonic Inlet During Throat Regulation," *Chinese Journal of Aeronautics*, Vol. 36, No. 11, 2023, pp. 135–152.
https://doi.org/10.1016/j.cja.2023.08.004

[11] Mitani, T., Sakuranaka, N., Tomioka, S., and Kobayashi, K., "Boundary-Layer Control in Mach 4 and Mach 6 Scramjet Engines," *Journal of Propulsion and Power*, Vol. 21, No. 4, 2005, pp. 636–641.
https://doi.org/10.2514/1.7978

[12] Wang, J. Y., Xie, L. R., Zhao, H., Teng, Y. L., and Ma, G. F., "Fluidic Control Method for Improving the Self-Starting Ability of Hypersonic Inlets," *Journal of Propulsion and Power*, Vol. 32, No. 1, 2016, pp. 153–160.
https://doi.org/10.2514/1.B35749

[13] He, Y. B., Chang, J. T., Bao, W., Huang, H. Y., and Yu, D. R., "Numerical Investigation of Local Resistance to Backpressure in Hypersonic Inlet with Suction," *Journal of Propulsion and Power*, Vol. 32, No. 6, 2016, pp. 1531–1543.
https://doi.org/10.2514/1.B36043

[14] Jin, Y. C., and Yao, W., "Comprehensive Assessments of Hypersonic Inlet Restart Using Active Jet," AIAA Paper 2023-4444, June 2023.
https://doi.org/10.2514/6.2023-4444

[15] Kantrowitz, A., and Donaldson, G., "Preliminary Investigation of Supersonic Differs," NACA WRL-713, 1945.

[16] Veillard, X., Tahir, R., Timofeev, E., and Mölder, S., "Limiting Contractions for Starting Simple Ramp-Type Scramjet Intakes with Overboard Spillage," *Journal of Propulsion and Power*, Vol. 24, No. 5, 2008, pp. 1042–1049.
https://doi.org/10.2514/1.34547

[17] Moradian, N., and Timofeev, E., "Starting Characteristics of Prandtl-Meyer Scramjet Intakes with Overboard Spillage," *Journal of Propulsion and Power*, Vol. 24, No. 5, 2018, pp. 189–197.
https://doi.org/10.2514/1.B36574

[18] Flock, A. K., and Gülhan, A., "Modified Kantrowitz Starting Criteria for Mixed Compression Supersonic Intakes," *AIAA Journal*, Vol. 57, No. 5, 2019, pp. 2011–2016.
https://doi.org/10.2514/1.J057283

[19] Janakiram, S., Kumar, G., Sinha, K., and Duvvuri, S., "Starting Characteristics of Curved Compression Ramp Air Intakes with Overboard Spillage," *AIAA Journal*, Vol. 62, No. 3, 2024, pp. 1066–1020.
https://doi.org/10.2514/1.J063281

[20] Xie, W. Z., Ma, G. F., Guo, R. W., Chen, H., Wen, Y. F., and Guo, S. M., "Flow-Based Prediction for Self-Starting Limit of Two-Dimensional Hypersonic Inlets," *Journal of Propulsion and Power*, Vol. 32, No. 2, 2016, pp. 463–471.
https://doi.org/10.2514/1.B35703

[21] Yang, S. Z., Xie, W. Z., Xu, C. L., and Ma, G. F., "Generalized Prediction for Self-Starting Performance of Two Dimensional Hypersonic Inlets," *Physics of Fluids*, Vol. 36, No. 1, 2024, Paper 015129.
https://doi.org/10.1063/5.0174803

[22] Liu, X., Liang, J. H., and Wang, Y., "Research on the Effect of Cowl Lip Angle on the Accelerating Start Process of a Two-Dimensional Hypersonic Inlet," *Proceedings of the Institution of Mechanical Engineers, Part G: Journal of Aerospace Engineering*, Vol. 230, No. 14, 2016, pp. 2615–2627.
https://doi.org/10.1177/0954410016629691

[23] Tong, X. T., Yue, L. J., and Chen, H., "Similarity Analysis for Two-Dimensional Hypersonic Inlets Restart," *AIAA Journal*, Vol. 61, No. 10, 2023, pp. 4230–4246.
https://doi.org/10.2514/1.J062529

[24] Li, Z., Huang, B., Yang, J., Wei, Y., Liu, X., and Liu, J., "Starting Characteristics of Hypersonic Inlets in Shock Tunnel," *28th International Symposium on Shock Waves*, edited by K. Kontis, Springer, Berlin, Heidelberg, 2012, pp. 1015–1020.
https://doi.org/10.1007/978-3-642-25685-1_154

[25] Yue, L. J., Jia, Y. N., Xu, X., Zhang, X. Y., and Zhang, P., "Effect of Cowl Shock on Restart Characteristics of Simple Ramp Type Hypersonic Inlets with Thin Boundary Layers," *Aerospace Science and Technology*, Vol. 74, 2018, pp. 72–80.
https://doi.org/10.1016/j.ast.2017.12.018

[26] Chang, J. T., Yu, D. R., Bao, W., Fan, Y., and Shen, Y., "Effects of Boundary-Layers Bleeding on Unstart/Restart Characteristics of Hypersonic Inlets," *Aeronautical Journal*, Vol. 113, No. 1143, 2009, pp. 319–327.
https://doi.org/10.1017/S0001924000002992

[27] Fan, Y., Chang, J. T., and Bao, W., "Effects of Wall Temperature on Unstart/Restart Characteristics of Hypersonic Inlet," *Journal of Solid Rocket Technology*, Vol. 32, No. 3, 2009, pp. 266–270 (in Chinese).

[28] You, J., Xia, Z. X., Wang, D. P., and Fang, C. B., "Numerical Study on Influencing Factors of Restarting Characteristics for a Hypersonic Inlet," *Journal of Solid Rocket Technology*, Vol. 34, No. 5, 2011, pp. 161–166 (in Chinese).

[29] Li, Z. F., Gao, W. Z., and Yang, J. M., "Numerical and Experimental Investigation for Starting Characteristics of a Two-Dimensional Inlet," *Journal of Propulsion Technology*, Vol. 37, No. 7, 2016, pp. 1224–1232 (in Chinese).
https://doi.org/10.13675/j.cnki.tjjs.2016.07.004.

[30] Guo, S. T., Li, Z. F., Gao, W. Z., and Yang, J. M., "Analogy Between Effects of Attack Angle and Mach Number on Inlet Starting," *Journal of Propulsion Technology*, Vol. 38, No. 5, 2017, p. 983 (in Chinese).
https://doi.org/10.13675/j.cnki.tjjs.2017.05.004

[31] Su, W. Y., Hu, Z. W., Tang, P. P., and Chen, Y., "Transient Analysis for Hypersonic Inlet Accelerative Restarting Process," *Journal of Spacecraft and Rockets*, Vol. 54, No. 2, 2017, pp. 376–385.
https://doi.org/10.2514/1.A33601

[32] Xie, W. Z., Jin, Y., Ge, Y., Yang, S. Z., Zeng, C., and Guo, S. M., "Feasibility of Employing the Restarting Process to Evaluate the Self-Starting Ability for Hypersonic Inlets," *Aerospace Science and Technology*, Vol. 107, 2020, Paper 106347.
https://doi.org/10.1016/j.ast.2020.106347

[33] Jin, Y., Sun, S., Tan, H., Zhang, Y., and Huang, H., "Flow Response Hysteresis of Throat Regulation Process of a Two-Dimensional Mixed-Compression Supersonic Inlet," *Chinese Journal of Aeronautics*, Vol. 35, No. 3, 2022, pp. 112–127.
https://doi.org/10.1016/j.cja.2021.06.013

[34] Mölder, S., Timofeev, E., and Tahir, R., "Flow Starting in High Compression Hypersonic Air Inlets by Mass Spillage," AIAA Paper 2004-4130, July 2004.
https://doi.org/10.2514/6.2004-4130

[35] Sun, B., and Zhang, K. Y., "Empirical Equation for Self-Starting Limit of Supersonic Inlets," *Journal of Propulsion and Power*, Vol. 26, No. 4, 2010, pp. 874–875.
https://doi.org/10.2514/1.46798

[36] Jia, Y. N., Yue, L. J., and Chang, X. Y., "The Phenomena of Sudden Change in Hypersonic Inlets Self-Starting Capability," AIAA Paper 2017-2188, March 2017.
https://doi.org/10.2514/6.2017-2188

[37] Chang, J. T., Yu, D. R., Bao, W., and Qu, L., "Influence Factors of Unstart Boundary for Hypersonic Inlets," AIAA Paper 2008-4586, July 2008.
https://doi.org/10.2514/6.2008-4586.

[38] Tong, X. T., Yue, L. J., Chen, H., Zhang, Q. F., and He, C. M., "Similarity Analysis on Two-Dimensional Hypersonic Inlets Unstart," *AIAA Journal*, Vol. 61, No. 2, 2023, pp. 555–572. https://doi.org/10.2514/1.J061874

[39] Tong, X. T., Yue, L. J., Wu, W. N., Zhang, Q. F., and Chen, H., "Self-Similar Unstart Characteristics of Supersonic Contraction Duct with an Expansion Corner," *Physics of Fluids*, Vol. 36, No. 1, 2024, Paper 016148. https://doi.org/10.1063/5.0180243

[40] Barenblatt, G. I., *Scaling, Self-Similarity, and Intermediate Asymptotics*, Cambridge Univ. Press, Cambridge, England, U.K., 1996, pp. 145–160.

[41] Watanabe, R., Ishii, T., Hirono, Y., and Maruoka, H., "Data-Driven Discovery of Self-Similarity Using Neural Networks," *Physical Review E*, Vol. 111, No. 2, 2025, Paper 024301. https://doi.org/10.1103/PhysRevE.111.024301

[42] Zhang, Y., Tan, H. J., Zhuang, Y., and Wang, D. P., "Influence of Expansion Waves on Cowl Shock/Boundary Layer Interaction in Hypersonic Inlets," *Journal of Propulsion and Power*, Vol. 30, No. 5, 2014, pp. 1183–1191. https://doi.org/10.2514/1.B35090

[43] Souverein, L. J., Bakker, P. G., and Dupont, P., "A Scaling Analysis for Turbulent Shock-Wave/Boundary-Layer Interactions," *Journal of Fluid Mechanics*, Vol. 714, 2013, pp. 505–535. https://doi.org/10.1017/jfm.2012.495

[44] Wang, Z. G., Zhao, Y. L., Zhao, Y. X., and Fan, X. Q., "Prediction of Massive Separation of Unstarted Inlet via Free-Interaction Theory," *AIAA Journal*, Vol. 53, No. 4, 2015, pp. 1108–1111. https://doi.org/10.2514/1.J053501

V. Raman
Associate Editor